

Available online at [www.sciencedirect.com](http://www.sciencedirect.com)

**jmr&t**  
Journal of Materials Research and Technology  
journal homepage: [www.elsevier.com/locate/jmrt](http://www.elsevier.com/locate/jmrt)



## Original Article

# Laser powder bed fusion of Alumina/Fe–Ni ceramic matrix particulate composites impregnated with a polymeric resin



Mohammad Azami <sup>a</sup>, Armin Siahsharani <sup>a</sup>, Amir Hadian <sup>b</sup>, Zahra Kazemi <sup>c</sup>, Davood Rahmatabadi <sup>a</sup>, Seyed Farshid Kashani-Bozorg <sup>d</sup>, Karen Abrinia <sup>a,\*</sup>

<sup>a</sup> School of Mechanical Engineering, College of Engineering, University of Tehran, Tehran, 11155-4563, Iran

<sup>b</sup> Empa - Swiss Federal Laboratories for Materials Science and Technology, Uberlandstrasse 129, CH-8600 Dübendorf, Switzerland

<sup>c</sup> Institute for Aerospace Studies, University of Toronto, Dufferin Street 4925, M3H 5T6, Canada

<sup>d</sup> School of Metallurgy and Materials Engineering, College of Engineering, University of Tehran, Tehran, 11155-4563, Iran

## ARTICLE INFO

## Article history:

Received 31 December 2022

Accepted 24 March 2023

Available online 30 March 2023

## Keywords:

Additive manufacturing

Laser powder bed fusion

Ceramic matrix composites (CMCs)

Metallic particulates

Alumina

## ABSTRACT

Additive Manufacturing (AM) plays a key role in meeting the vital demands of Industry. The AM industry needs the range of applicable materials to be expanded by conducting research on novel ones. In the present investigation, alumina/Fe–Ni (steel) ceramic matrix particulate composite was fabricated employing laser powder bed fusion (LPBF) additive manufacturing (AM) technology. The quality of the printed samples was associated with the LPBF process parameters, which were optimized for this process. In general, the fabricated samples showed a microstructure of alumina matrix with uniform distribution of steel (Fe–Ni) particles. The as-printed samples exhibited pores. Thus, they were subjected to a sintering heat treatment cycle under an inert atmosphere. Although the sintering cycle considerably increased the average Vickers hardness, pores were not eliminated entirely. Therefore, polymer impregnation of the as-sintered samples was carried out to reduce porosities and microcracks. The mercury porosimeter showed that the porosity decreased sequentially after sintering and polymer impregnation. In addition, mechanical investigations revealed that the polymer impregnation improved the compressive strength of the sintered samples (from 56 to 120 MPa). Alumina-based materials find wide applications in various fields, including the manufacturing of electronic components, cutting tools, biomedical implants, and catalyst converters, owing to their low density, high hardness, wear and corrosion resistance, and biocompatibility. This study presents a viable approach for the fabrication of these materials, with developed samples exhibiting promising properties. The study emphasizes the potential of additive manufacturing as an approach for the fabrication of ceramic matrix composites reinforced with metallic particulates in future research.

© 2023 The Authors. Published by Elsevier B.V. This is an open access article under the CC BY license (<http://creativecommons.org/licenses/by/4.0/>).

\* Corresponding author.

E-mail address: [Cabrinia@ut.ac.ir](mailto:Cabrinia@ut.ac.ir) (K. Abrinia).

<https://doi.org/10.1016/j.jmrt.2023.03.181>

2238-7854/© 2023 The Authors. Published by Elsevier B.V. This is an open access article under the CC BY license (<http://creativecommons.org/licenses/by/4.0/>).

## 1. Introduction

Ceramic matrix composites (CMCs) are a frequently used category of materials in nowadays high-tech industries [1,2]. Ceramic-metals, also called cermet, are a prominent sub-category of CMCs, which can be a solution for ceramic-property limitations such as brittle failure, low fracture toughness, and sensitivity to thermal shock [3,4]. They are widely used in space vehicles, gas turbines, automotive parts, slide bearings, etc. [5–7]. Alumina is one of the commonly used ceramics in the fabrication of CMCs [8], which is proven to encompass impressive behavior at elevated temperatures, excellent thermal conductivity, high hardness, significant corrosion, wearing and abrasion resistance, and relatively low density (nearly half of that of steel) [9]. Alumina is an ideal material for high-temperature insulators, substrates, and circuit boards [10]. Also, the high hardness and wear resistance of alumina or alumina-based composites, makes them ideal for use in cutting tools or high-resistance coatings, especially when heat resistance is required [11]. Moreover, alumina is biocompatible, which means it can be used in medical implants without causing an immune response. Porous alumina-based implants are used in hip and knee replacements, dental implants, and other medical applications [12,13]. Porous alumina-based materials are also widely used as catalyst converters or to purify air or water [14,15].

On the other hand, alumina is an excellent candidate to combine with steel, considering the importance of various types of steel in industries [16]. For instance, SiC/steel composites are almost impossible to fabricate, as the oxide coatings on SiC are not protective enough to shield the ceramic against corrosion caused by the melted metal. Therefore, the dissolution of SiC in the melt occurs. Consequently, alumina as an oxide ceramic is a well-deserved option to compound with high-melting alloys (e.g., steels or Ni-based superalloys). In such composites, the interface of steel-alumina has proven to show satisfactory bonding, with no cracks [17–19].

Koopmann et al. [20] also demonstrated that the good interface behavior of alumina-steel can be observed even for additively manufactured samples. Moreover, for high-tech applications, there is an increasing necessity to develop novel materials specifically designed for exclusive purposes [21,22]. To this end, various innovative materials, particularly composites, were introduced through different fabrication techniques [23–25]. Considering the broad utilization of alumina in industries, a favorable category of composites can be achieved by developing alumina/metallic composites. It enables us to obtain superior material behavior, encompassing selected properties of alumina and metals (e.g., metals act as the reinforcement phase or a coolant agent in the structure, and alumina adds high abrasion resistance to it, etc.).

Such composites can also be produced through powder metallurgy (PM) [26], hot pressing (HP) [27], hot isostatic pressing (HIP) [28], spark plasma sintering (SPS) [29], and casting methods [30]. However, fabrication of the CMCs via conventional techniques can be costly and geometrically limited. Besides, the aforementioned processes sometimes prolong the path to the desired parts. To overcome these barriers, additive manufacturing (AM) techniques can be introduced as an alternative solution to produce CMCs [31]. In these methods, the components are produced through a layer-upon-layer material deposition until the desired shape is made [32]. It is required to study the potential of AM to produce CMCs. The additively manufactured CMC samples were also compared to those fabricated through conventional techniques [33–35]. One major AM category is laser powder bed fusion (LPBF), in which a laser beam is utilized to selectively melt or sinter and fuse the powder particles [36]. The principle of this method is that a thin layer of powder is uniformly deposited on the printing bed through a blade coater. The laser beam scans the selected area via the intended parameters and the desired scanning pattern. The adjacent powders are then fused together under the influence of the heat induced by the laser beam. Subsequently, the printing bed moves downwards on the z-axis, and another layer of

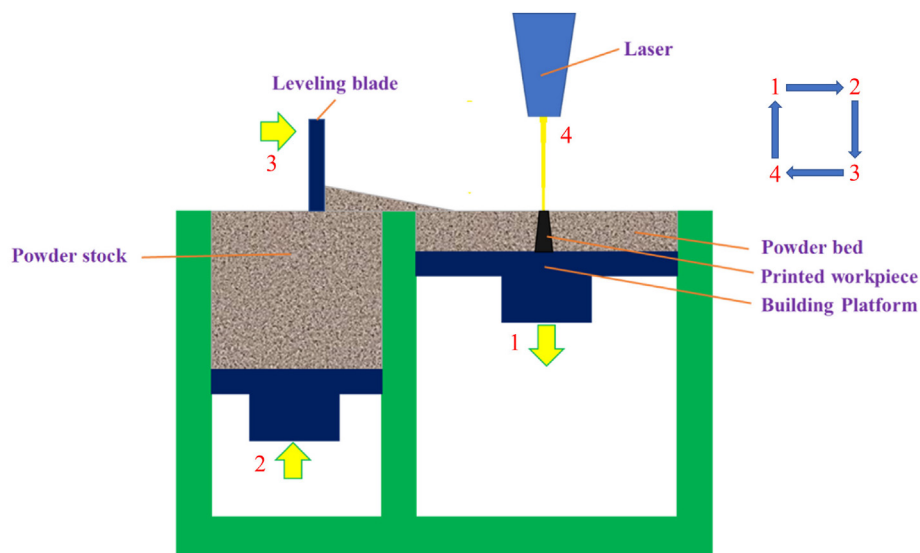


Fig. 1 – Schematic representation of the LPBF process.

powder is coated on the top. This procedure is repeated until the final geometry is obtained. The schematic illustration of the LPBF process is shown in Fig. 1. Despite considerable advancement in this area, the LPBF technique is still in the early stages of development. A considerable number of researches were carried out to develop new materials for the LPBF, including iron-based alloys [37,38], aluminum-based alloys [39–41], metal-ceramic composites [42–44], and metal matrix composites [45–48].

During the past few years, a limited number of researches are conducted on AM of metal-reinforced CMCs, most of which are associated with AM of WC-Co composites. In literature, LPBF [49–51], direct laser deposition [52], binder jetting [53,54], and laser engineering net shaping (LENS) [55,56] AM techniques have been used to fabricate CMCs. Among the mentioned techniques, LPBF includes most of the research. A major problem in LPBF of the metal-reinforced CMCs is the formation of cracks due to the thermal gradients [57]. Grigoriev et al. [50] used LPBF to additively manufacture WC-6 wt % Co samples and reported crack formation, which is attributed to the significant difference between the melting point of the ceramic and the metal. Khmyrov et al. [58] studied the formation of various phases during the LPBF of WC with different Co contents (6, 50, 72.4, and 75 wt%). They reported the presence of WC and the formation of  $W_2C$  in the structure for samples with 6 wt% Co. For any other sample, they observed a full dissolution of WC. A small amount of  $W_4Co_2C$  was revealed in samples containing 75 and 72.4 wt% Co, while samples with 50 wt% Co contained  $W_3Co_3C$ .

On the other hand, some difficulties are faced in the laser processing of ceramics related to their low optical absorption coefficient and, subsequently, the problematic absorbing ratio of the laser energy during the process. Compounding the ceramic with metal particles is an effective solution to enhance light absorption. Besides, ceramics usually have high melting points and do not melt during laser processing. As a result, they do not have the proper flowability to fill the pores during printing. Adding metallic particles to ceramics can reduce the porosity ratio, as the metals have the potential to melt, flow, and fill the gaps at lower melting temperatures.

With regard to the reasons mentioned above, this research aimed to additively manufacture the alumina/standard EOS steel alloy (DS20) composite through the LPBF technique. It is worth noting that parameters such as flowability, density, size, shape, and conductivity of the powder are critical

characteristics in the broad implementation of the technique. After accomplishing the manufacturing phase, the samples' microstructure variation, porosity analysis, hardness testing, and compressive strength were addressed. Alumina-based materials have a broad range of industrial applications, especially alumina/metal composites. Previous research by Koopmann et al. [20] reported zirconia-alumina ceramic coating on a steel substrate. However, to our knowledge, this study presents the first development of an alumina/steel ceramic matrix composite using LPBF, demonstrating the feasibility of printing cermet. The advantages of additive manufacturing, including design flexibility, energy efficiency, and reduced post-processing and machining requirements, make this breakthrough approach a promising option for the fabrication of alumina-based materials. This research offers new avenues for the additive manufacturing of ceramic-based materials in general.

## 2. Materials and methods

### 2.1. Material

To prepare the composite powder, an aluminum oxide powder (GF54503557, Aldrich, United States) and a standard EOS steel alloy (DS20, EOS GmbH, Germany) powders were carefully sieved through a mesh size of  $<45\ \mu\text{m}$  to eliminate any agglomerated particles. Using a dry ball milling setup, the powders were mixed at a ratio of 80 wt% alumina and 20 wt% steel for 4 h. The composition of steel powder was investigated by the inductively coupled plasma–optical emission spectrometry (ICP-OES) analysis through the Sciex Elan 6100 (PerkinElmer, USA) system.

### 2.2. Processing

A direct metal laser sintering (DMLS) machine (M250 XTENDED DMLS 3D printer, EOS GmbH, Germany) was used to fabricate alumina/steel cylindrical specimens with a diameter and height of 5 and 15 mm, respectively. The optimal printing parameters (Table 1), including laser power, laser scanning speed, layer thickness, scanning pattern, and hatch space, were adjusted, starting with the values derived from previous

**Table 1 – DMLS process parameters for additive manufacturing of alumina-EOS DS20 steel cylindrical specimens.**

Parameter	Value
Laser Power	190 W
Laser scanning speed	550 mm/s
Layer thickness	30 $\mu\text{m}$
Hatch space	150 $\mu\text{m}$
Scanning pattern	Sorted
Powder bed temperature	170 $^{\circ}\text{C}$
Atmosphere	Argon
Building Direction	90 $^{\circ}$
Geometry	Cylinder

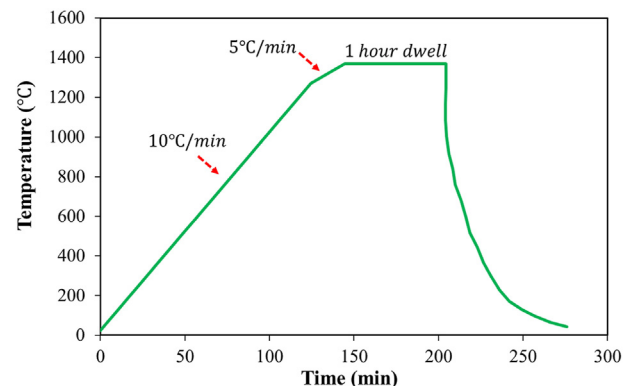


**Fig. 2 – The heating program used for the sintering of the as-printed specimens.**

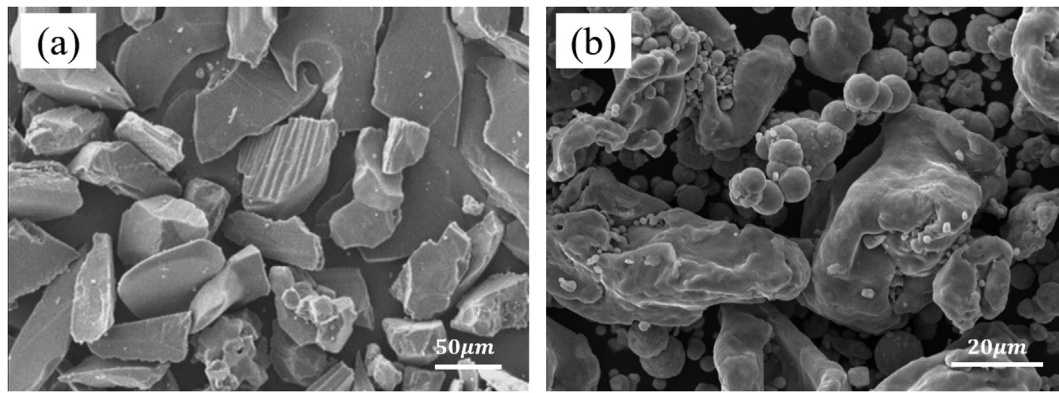


**Fig. 3 – SEM micrograph of the (a) as-received  $\text{Al}_2\text{O}_3$  powder and (b) as-received EOS DS20 steel powder.**

studies [59]. The as-printed specimens were then sintered in a graphite furnace under an inert gas (argon) atmosphere to improve the bonding within the structure. The sintering heating program is presented in Fig. 2.

After the sintering process, a polymeric resin (Dichtol WTF 1532, Metaplastic, Germany) was used to infiltrate into the cracks and pores of the specimens. According to the data provided by the resin manufacturer, Dichtol polymer has a service temperature of  $-40\text{ }^{\circ}\text{C}$  to  $+300\text{ }^{\circ}\text{C}$ . In addition, the low viscosity of the resin at room temperature could enhance the infiltration process. For the infiltration process, specimens were immersed in the liquid resin for 60 min and then cured for 4 h at room temperature according to the guideline provided by the manufacturer. This process was repeated three times to ensure complete penetration of the resin.

### 2.3. Characterization

Simultaneous thermal analysis (STA 504, BÄHR-Thermoanalyse GmbH, Germany) up to  $1600\text{ }^{\circ}\text{C}$  and in an argon atmosphere was used to investigate the steel powder's thermal properties and determine a suitable sintering temperature.

Microstructural studies were performed on both as-received powders and processed samples (as-printed, as-sintered, and polymer-impregnated). Field-emission scanning electron microscopy (FE-SEM) (Mira3, TESCAN, Czech Republic) was used to study the polished cross-sections and the fracture surface of the fabricated specimens. In addition, an energy-dispersive x-ray spectrometer (EDS) was utilized to characterize their chemical compositions.

Mercury porosimetry distribution analysis was conducted in two different ranges. To investigate the distribution of pores below  $D: 10\text{ }\mu\text{m}$  and pores above  $D: 10\text{ }\mu\text{m}$ , a Pascal 440 and a Pascal 140 Mercury Porosimeters (Thermo Fisher Scientific, United States) were used, respectively.

To evaluate the mechanical properties, cylindrical samples with a diameter and height of 5 and 7.5 mm, respectively, were prepared and subjected to the compression test using a universal testing machine (2000KPX, Instron, United States); the

test was conducted in accordance with the ASTM-C1424 standard at a 1 mm/min rate for all samples. The as-fractured samples were studied to investigate the fracture behavior. To check the hardness of the specimens, a Vickers microhardness indenter was used (MMT-X, Matsuzawa, Japan) under a force and duration of 50 g and 20 s, respectively. The microhardness test was carried out at different locations along the surface of the specimens with a spacing distance of  $500\text{ }\mu\text{m}$  between adjacent indentation points.

## 3. Results and discussion

### 3.1. Characteristics of the as-received powder materials

Powder characteristics, including morphology and particle size, were studied using FE-SEM (Fig. 3). The as-received alumina particles showed an elongated polygonal shape, and most of the particles were in the range of  $30\text{--}45\text{ }\mu\text{m}$  (Fig. 3(a)). The DS20 steel particles exhibited a spherical morphology with an average particle size below  $20\text{ }\mu\text{m}$ . Some agglomerates could be noted in the initial steel powder, which could be removed by ball milling and sieving (Fig. 3(c)). The relatively small diameter of the steel particles and their large specific surface area led to the enhancement in light absorption properties during DMLS, which raised the heat of the particles and facilitated the sintering properties. Furthermore, the spherical morphology of the metal particles could lead to a smoother and more uniform layer during the powder deposition [60].

The composition of DS20 steel powder obtained from ICP-OES analysis is listed in Table 2.

The homogenous distribution of steel particles in the dominant  $\text{Al}_2\text{O}_3$  powder was found using SEM of the as-milled powder mixtures (Fig. 4). The even distribution was necessary to increase the laser absorption rate and enhance the mixture's flowing characteristic during the printing process. It could also improve liquid wetting characteristics and reordering of the particles.

**Table 2 – Composition of the steel powder used in this study, obtained from ICP-OES analysis.**

Element	Fe	Ni	Cu	Si	Mg	Al	P	Ti	Others
Weight (%)	Balance	21.89	7.48	0.028	0.026	0.026	0.030	0.033	< 0.060



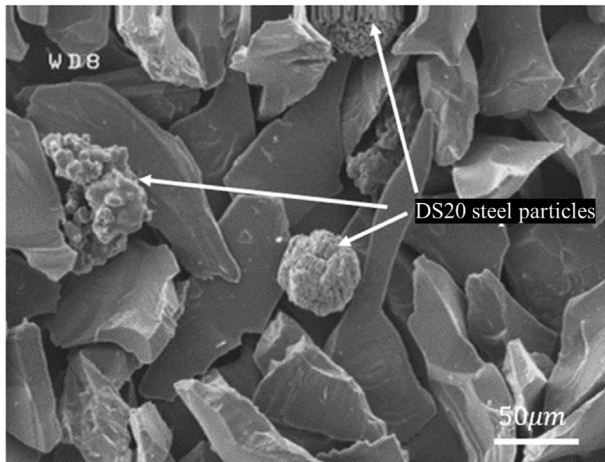


**Fig. 4 – SEM micrograph of the as-milled powder mixture.**

### 3.2. DMLS processing and sintering

Different powder ratios were investigated to obtain the optimum mass ratio of each component in the fabricated specimens. Any defective ones with visible cracks or large porosities were ruled out. The printed specimen with the composition of 80 wt% of  $\text{Al}_2\text{O}_3$  powder and 20 wt% of the DS20 steel particles showed no visible defects. The DMLS process parameters were also determined. Different parameters, including the laser scan pattern, laser energy density, and heat treatment program, were selected as variables, and optimum parameters were obtained based on the printed specimens' characteristics, which are reported in Table 2. Then, the DMLS was successfully used to manufacture cylindrical specimens with the mentioned composition. The fabricated cylindrical specimens are shown in Fig. 5.

The sintering process was then conducted to improve the strength of the as-printed cylinders and relieve their associated residual stresses that formed due to fast localized cooling during printing [61]. The sintering temperature for alumina was determined in different works to be about 1300 °C–1600 °C [62]. However, due to the existence of the metallic component in the CMC structure, the melting point of this component played an important role in determining its sintering temperature. To select a suitable maximum temperature for the sintering phase, the STA analysis was performed on the steel powder, presented in Fig. 6. Based on the signals, an endothermic peak is evident at 1370°, possibly associated with the liquid formation. Accordingly, this temperature (1370°) was selected for the sintering process.

### 3.3. Microstructural characterization of the as-printed, as-sintered, and polymer-impregnated samples

Fig. 7 displays backscattered electron (BSE) SEM micrographs of the polished surface of the samples. The as-printed sample showed uniform distribution with no accumulation of the steel particles over the  $\text{Al}_2\text{O}_3$  matrix. Besides, the diffusion of the steel alloys in the  $\text{Al}_2\text{O}_3$  matrix is not evident from the images (Fig. 7(b)). The as-printed body is a porous structure and contains micro-cracks mainly formed between the porosities. From the fracture cross-section (Fig. 8(a)), it can be observed that these cracks can propagate through the structure when the load is applied. The formation of micro-cracks in the sample is attributed to the brittleness of the alumina matrix and the differences in melting points and thermal expansion coefficients of alumina and steel components [51,63]. Due to the weak adhesion between steel and alumina matrix, steel particles were removed during polishing in some areas; these are distinguished in dark circles in the micrograph. It also can be understood from Fig. 7(c) that some of the alumina particles were melted during the printing process. A similar effect was noted on the fracture surface of the bars, as highlighted in Fig. 8(a). Besides, a long crack formed due to thermal gradients during solidification. Fig. 7(d–f) illustrates BSE images of the sintered sample.

The images of the as-printed and as-sintered samples show no discernible difference between them. Due to the existence of the steel component in the fabricated composite and considering the steel area being melted at 1370 °C, liquid phase sintering must have occurred during the heat-treatment to achieve full densification. However, the mentioned phenomenon did not happen because of the poor wettability of the steel and alumina, the high interfacial energy between steel and alumina, and the presence of a thin layer of oxide on the surface of the steel, which prevents melted steel from moving between alumina particles [64–66]. From the fracture surface analysis (Fig. 8(c) and (d)), spherical steel particles can still be observed, confirming the stated phenomenon. It is evident from the SEM images of the polished cross-section that the melted metallic particles did not rearrange the alumina particles due to capillary action. On the other hand, it could be noticed that the as-sintered samples have relatively higher densification than the as-printed body. The reason could be associated with the densification of the alumina component during sintering. The onset of sintering temperature for alumina is around 1000 °C. Hence, alumina particles started to densify at this temperature through the solid-state sintering mechanism. Since the sintering

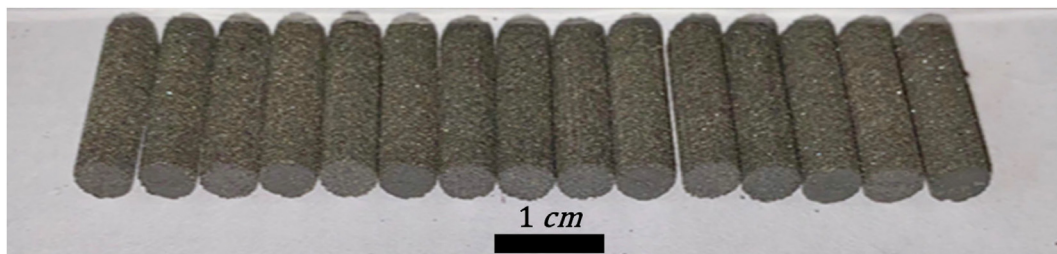


**Fig. 5 – The as-printed cylindrical specimens with the composition of 80% alumina-20% DS20 steel (wt%).**

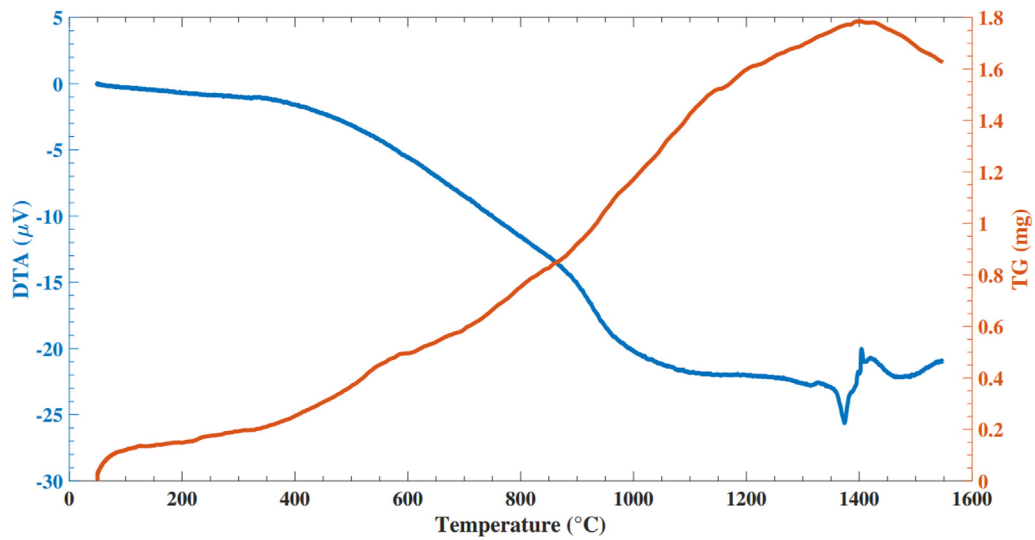


Fig. 6 – STA analysis of the DS20 steel powder, based on TG and DTA signals.

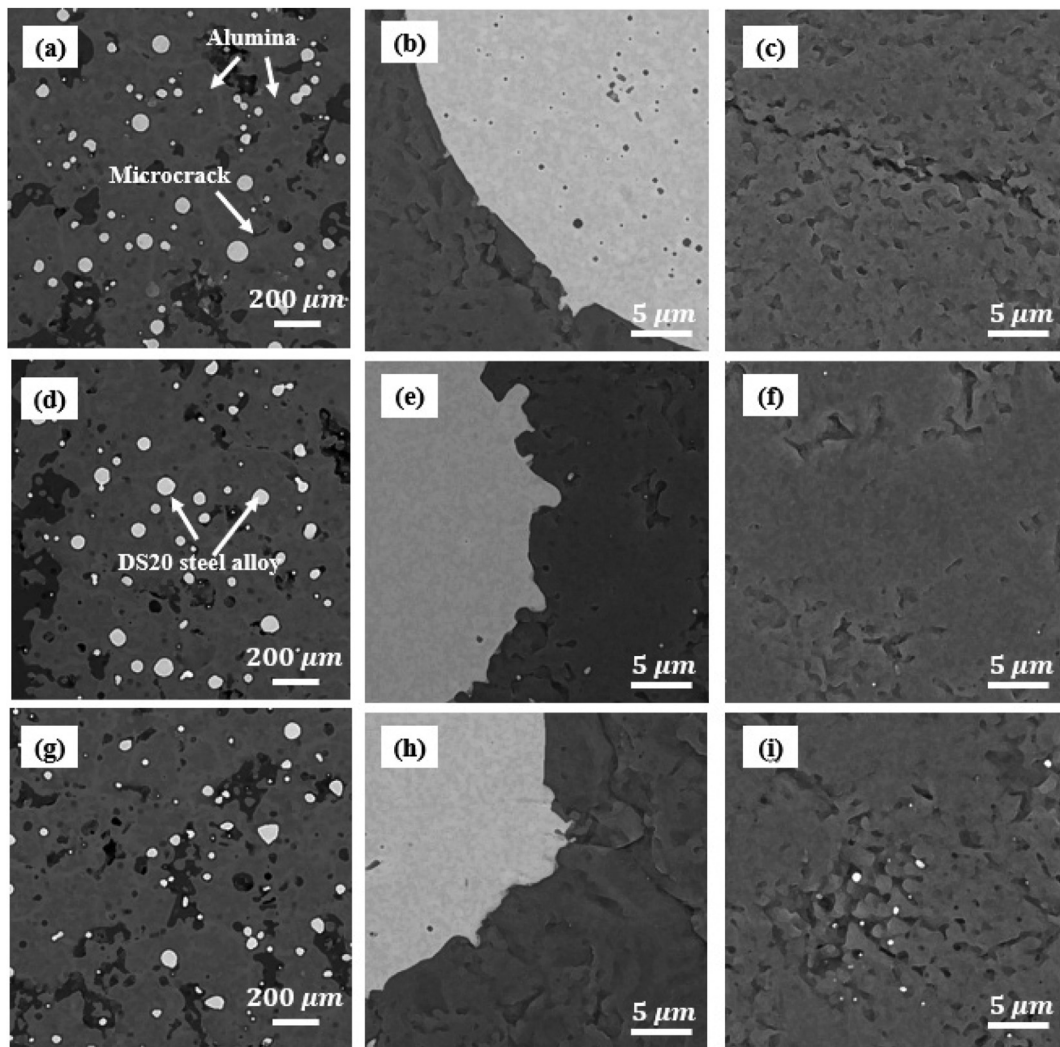
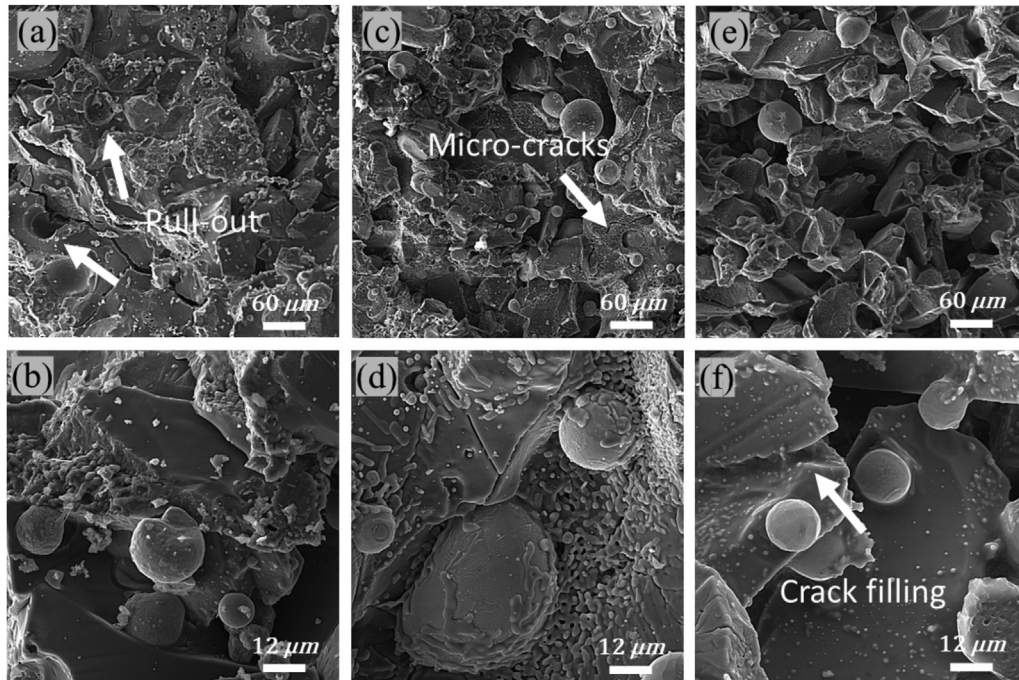


Fig. 7 – Backscattered electron SEM micrographs of the samples, the interaction of the steel with ceramic areas and ceramic section (a–c) as-printed; (d–f) as-sintered; and (g–i) polymer-impregnated.



**Fig. 8 – Secondary electron SEM micrographs of the fracture cross-section of the samples (a and b) as-printed; (c and d) as-sintered; and (e and f) polymer-impregnated.**

temperature of the CMC was selected to be at 1370 °C, which was 370 °C higher than the onset of the sintering temperature of alumina, more densification was expected. However, the complete densification of the CMC was not achieved since the ideal sintering temperature of alumina is between 1500 and 1700 °C, which was impossible to implement due to the presence of the metal in the structure. Considering the STA analysis of the metallic phase (Fig. 6), the formation of gas at temperatures above 1370 °C could introduce defects into the structure. The incomplete densification of alumina may also be linked to the sintering atmosphere chosen. This is because argon has a lower solubility in alumina than oxygen, which may lead to less efficient sintering [67]. It is worth noting that a noble gas was chosen as the atmosphere due to the presence of metallic particles, and the risk of oxidation during sintering, which could have had a detrimental effect. It should be considered that solidification occurred so fast when the alumina particles were melted during the printing process. So, densification could not be achieved entirely. Therefore, the particles only stuck together. By comparing the steel and alumina interaction for the as-printed body and the sintered samples in Fig. 7(b) and (e), it could be concluded that the pores inside the steel area are removed after sintering.

Despite performing the sintering process and the resultant relative increase in the strength of the areas, the samples remained brittle due to the porosities in their structures. So, they could not be used under relatively high mechanical loads. Therefore, an attempt was made to remove the cracks and reduce the porosity in the samples by penetrating a suitable polymer into the matrix to improve their strength. The specimens were immersed in the Dichtol WFT 1532 resin. This polymeric solution was specifically designed to fill the pores (0–0.1 mm) and subsequently cause an improvement in the

material's mechanical and corrosion behavior. The micrographs of the samples immersed in the resin, “the polymer-impregnated sample”, are shown in Fig. 7(g)–(i). From the polished cross-section, almost difference can be noted between the images of the samples before and after the polymer infiltration process. However, as highlighted in Fig. 8(f), the polymeric solution could close some micro-cracks due to the low viscosity and easy penetration characteristics. Larger cracks and porosities cannot be filled in, but a thin layer on the defects' walls can be formed, improving the properties. It is worth noting that while the sintering phase was unable to eliminate large pores or voids, it was a crucial step that could not be omitted. Laser Powder Bed Fusion (LPBF) only provided initial adhesion between the particles to form the desired geometry. Therefore, the as-printed samples had little strength, and sintering was necessary to enhance the particle bonding before polymer impregnation.

EDS was also employed to reveal elemental analysis and distribution of the elements within the microstructure after sintering the printed sample. The EDS analyses in three different regions of the sintered sample are shown in Fig. 9. In region A (Fig. 9), the highest weight percentages belong to Fe and Ni elements, which confirms the presence of DS20 steel alloy. This region also has C, O, Al, Si, P, and Cu in low percentages. About 90 wt% consists of Al and O in region B, proving this area comprises alumina. The other local elements are C, Si, P, Fe, Ni, and Cu, which possess 10 wt% of the composition. In region C, which is created during the printing process or due to the removal of steel areas during the polishing of samples, C and O have the highest weight percentages. For polishing, samples were cold-mounted using polymeric materials. This polymer can smear off from the cold mount during the polishing and penetrate through the



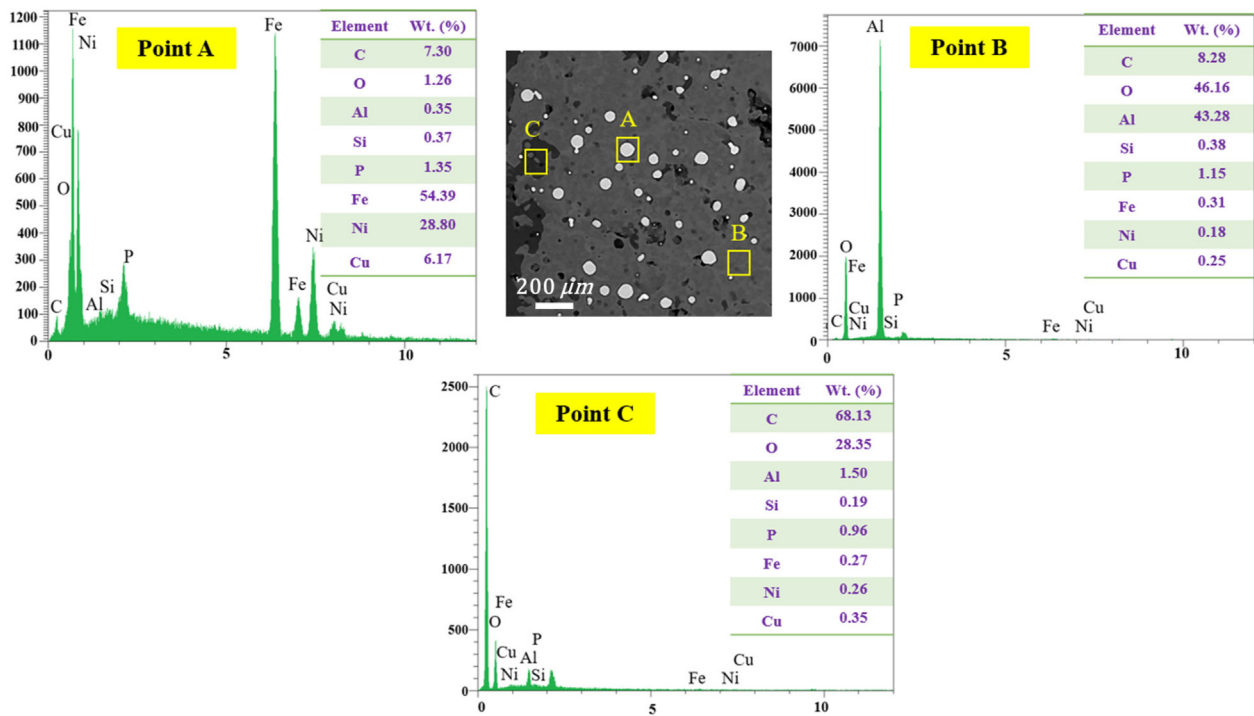


Fig. 9 – EDS analyses of the as-sintered alumina/steel composite.

porosities and cracks. This can be the reason for the existence of high contents of C and O in dark areas. All in all, EDS analyses of the different regions of the surface further revealed the poor diffusion of the molten steel inside the alumina during the printing and sintering processes.

EDS x-ray maps of the sintered sample are shown in Fig. 10. These maps show the distribution of the elements in the microstructure. As it is clear from the images, the steel alloy elements are distributed randomly and uniformly in the matrix. Furthermore, the semi-dendritic regions are enriched with alumina, which is caused by the non-equilibrium solidification of the composite during the DMLS process.

### 3.4. Porosity analysis

Fig. 11 presents the cumulative volume vs. the pore diameter for the as-printed and as-sintered samples before and after the polymer impregnation. The test was conducted in two ranges porosities of  $>10\ \mu\text{m}$  and  $<10\ \mu\text{m}$ . After sintering, the cumulative volume of the pores below  $10\ \mu\text{m}$  reduced by up to 16%. However, the cumulative volume of pores above  $10\ \mu\text{m}$  increased up to 17%, attributed to the higher thermal expansion of the metal components and causing new defects in the structure. Only a slight change in the overall percentage of porosities could be noted upon sintering the as-printed body,

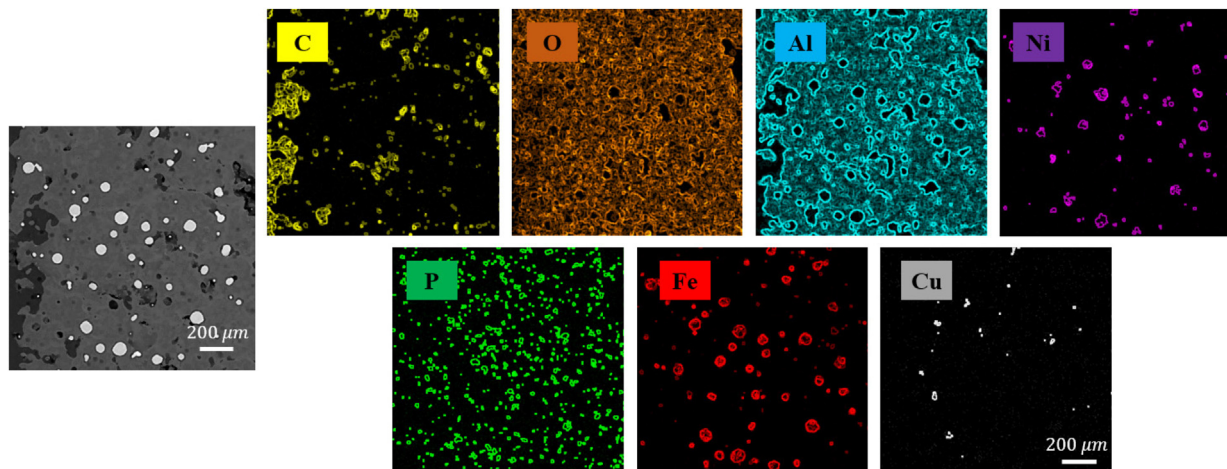


Fig. 10 – Backscattered electron SEM micrograph (a), and EDS X-ray maps of the as-sintered alumina/DS20 steel composite using C-K $\alpha$ , O-K $\alpha$ , Al-K $\alpha$ , Ni-K $\alpha$ , P-K $\alpha$ , Fe-K $\alpha$ , and Cu-K $\alpha$  radiations.



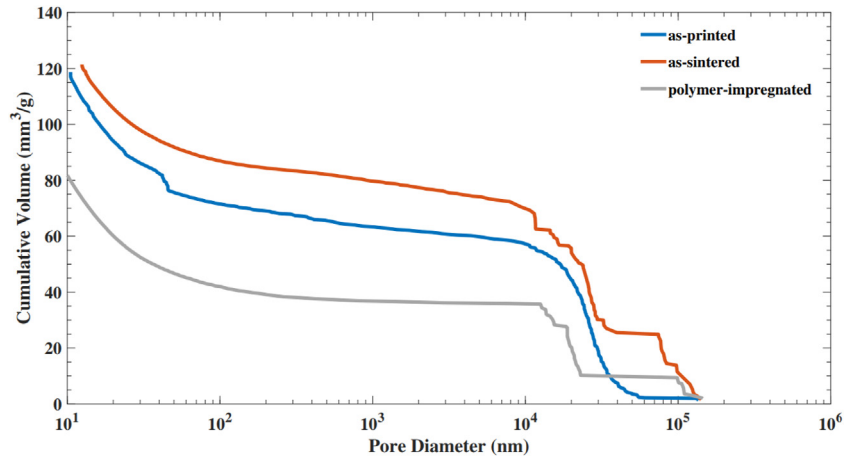


Fig. 11 – The cumulative volume of porosities in the as-printed, the as-sintered, and the polymer-impregnated samples.

which further ensured the poor wettability of alumina by steel alloy. Fig. 11 also displays that the cumulative volume of porosities below 10  $\mu\text{m}$  decreased up to 34% after immersing the samples in the polymeric resin, as the tiny pores and microcracks were filled during the infiltration. Moreover, polymer impregnation decreased the porosity related to the pores larger than 10  $\mu\text{m}$  by 31%. To summarize, the overall porosity percentage in the structure decreased from 36% to 27% after polymer infiltration. It should be mentioned that the goal of the polymer infiltration was to improve the fabricated composite's mechanical properties and corrosion behavior. Polymer impregnation did not aim to remove porosities entirely, as it would significantly increase the composite's weight. Besides that, it could noticeably reduce the heat transfer coefficient, which is considered a disadvantage as regards the application, requiring wear resistance and could lead to a considerable temperature increase in such processes. Finally, the main reason for the existence of porosities may relate to the irregular shapes of the initial alumina powder, which was also shown by Chen et al. [49]. The consequence of this problematic factor could be partially compensated if the wettability of alumina and the molten steel were sufficient to fill the matrix pores with steel.

### 3.5. Mechanical properties

Compression and Vickers microhardness tests were conducted to investigate the mechanical properties of the printed samples. Fig. 12 presents the microhardness test results of the as-printed and as-sintered samples. The as-sintered sample recorded higher microhardness values than the as-printed one, which is attributed to defining a proper sintering scenario. Owing to the elevated temperatures during the sintering process, the bonding of the ceramic particles happened suitably. This improved bonding could consequently lead to the reduction of the small pores and an increase in the hardness of the composite.

Moreover, the main reason the as-printed sample had more microcracks in the ceramic-metal interaction areas was their lower microhardness values [68]. Besides, the distribution of fine phases in the as-sintered composite was another critical contributing factor to the higher hardness values [57]. The results were consistent with other research works [69]. As it is clear from Fig. 12, the distribution of the microhardness value along the investigated line in the sintered sample is more uniform. This could be attributed to holding the sample at an elevated temperature for a long time in the sintering

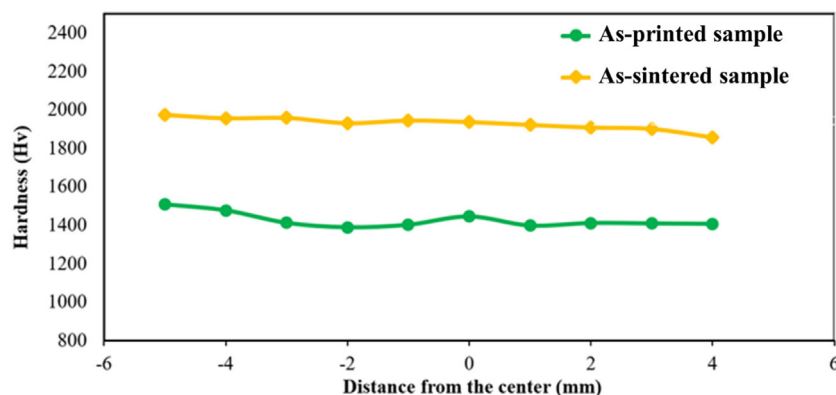
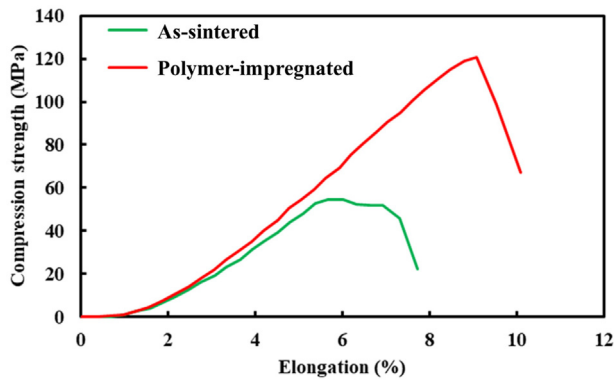


Fig. 12 – Variations of Vickers hardness in the as-printed and the as-sintered samples.



**Fig. 13 – Compression test curves of the as-sintered and the polymer-impregnated samples.**

process [70]. Due to the much lower hardness of the infiltrating polymer and its poor effect on the microhardness of the CMC, the microhardness values were not presented for the polymer-impregnated sample.

The results of the uniaxial compression test for both as-sintered and polymer-impregnated samples are presented in Fig. 13. As predicted, the polymer-impregnated sample showed a higher compressive strength. The slope of the compression-elongation curves in the elastic region is almost the same for both samples, indicating no considerable change in the compressive elastic modulus. The matrix-reinforcement interfaces and the porosity are two determinative factors for the compressive strength in CMCs. By immersing the as-sintered sample in the polymer, the compressive strength increased from 56 MPa to 120 MPa, indicating a sharp increase (more than twice). Polymer's presence improved the mechanical behavior of the composite by reducing the porosity, voids, and micro-cracks. The process of polymer impregnation managed to enhance the bonding between the ceramic grains by filling the gaps with the polymer, resulting in a stronger structure. The polymer was able to reinforce the ceramic material by providing extra strength and toughness. The polymer acts as a stress-relieving layer that disperses and absorbs stress, preventing cracks from spreading and improving the fracture toughness of the ceramic porous samples [71,72]. The polymer's role in enhancing ductility, toughness (the area under the stress-strain curve), and elongation is well-known.

#### 4. Conclusion

In summary, this study aimed to develop a composite material of alumina and Fe–Ni (steel) alloy using laser bed fusion additive manufacturing technology. The microstructural analysis showed a homogenous distribution of steel particles in the alumina matrix, demonstrating the effectiveness of the mixing strategy. Sintering the samples at 1370 °C improved the Vickers microhardness from approximately 1475 to 1960 HV, indicating enhanced mechanical properties due to better particle bonding. Despite this improvement, the samples still contained porosity and microcracks after

sintering. By utilizing polymer impregnation, the overall porosity was reduced from 36 to 27%, microcracks were eliminated, and the compressive strength increased sharply from 56 to 120 MPa, without any considerable weight gain or decrease in thermal isolation.

This research presents a practical method for manufacturing alumina-based materials, which have broad applications in areas like the fabrication of electronic components, cutting tools, biomedical implants, and catalyst converters due to their biocompatibility, low density, high hardness, and corrosion and wear resistance. The promising properties of the developed samples suggest that ceramic matrix composites reinforced by particulate metallic materials, in general, could be a promising research direction for materials development in additive manufacturing. Future research could explore the corrosion resistance of these samples and the possibility of scaling up production for industrial use.

#### Declaration of competing interest

The authors declare that they have no known competing financial interests or personal relationships that could have appeared to influence the work reported in this paper.

#### REFERENCES

- [1] Fu Z, Pang A, Luo H, Zhou K, Yang H. Research progress of ceramic matrix composites for high temperature stealth technology based on multi-scale collaborative design. *J Mater Res Technol* 2022;18:2770–83.
- [2] Xiong Y, Wang W, Jiang R, Huang B, Liu C. Feasibility and tool performance of ultrasonic vibration-assisted milling-grinding SiCf/SiC ceramic matrix composite. *J Mater Res Technol* 2022;19:3018–33.
- [3] Khaliq J. Ceramic matrix composites (CMCs). *Adv Mach Compos Mater* 2021:285–309.
- [4] Parsons E. Lightweight cellular metal composites with zero and tunable thermal expansion enabled by ultrasonic additive manufacturing: modeling, manufacturing, and testing. *Compos Struct* 2019;223:110656.
- [5] Zhu D. Aerospace ceramic materials: thermal, environmental barrier coatings and SiC/SiC ceramic matrix composites for turbine engine applications. 2018.
- [6] Padture N. Environmental degradation of high-temperature protective coatings for ceramic-matrix composites in gas-turbine engines. *Npj Mater Degrad* 2019;3:1–6.
- [7] Ahmadi M, Tabary SAAB, Rahmatabadi D, Ebrahimi MS, Abrinia K, Hashemi R. Review of selective laser melting of magnesium alloys: advantages, microstructure and mechanical characterizations, defects, challenges, and applications. *J Mater Res Technol* 2022;19:1537–62.
- [8] Cygan T, Wozniak J, Kostecki M, Petrus M, Jastrzebska A, Ziemkowska W, et al. Mechanical properties of graphene oxide reinforced alumina matrix composites. *Ceram Int* 2017;43:6180–6.
- [9] Zhang G, Liu Y, Lv Z, Wang J, Zhang W, Wu Y. Research on impact resistance of ceramic matrix composites. *Compos Struct* 2021;268:113977.
- [10] Lu G-Q, Yang W, Mei Y-H, Li X, Chen G, Chen X. Migration of sintered nanosilver on alumina and aluminum nitride

- substrates at high temperatures in dry air for electronic packaging. *IEEE Trans Device Mater Reliab* 2014;14:600–6.
- [11] Abu Bakar H, Fahmi N, Mokhtar F, Tamin N, Azlan U, Adam AA, et al. Fabrication and machining performance of powder compacted alumina based cutting tool. 2018.
  - [12] Xifre-Perez E, Ferre-Borull J, Pallares J, Marsal LF. Mesoporous alumina as a biomaterial for biomedical applications. *Open Mater Sci* 2015;2:13–32.
  - [13] Rahmati M, Mozafari M. Biocompatibility of alumina-based biomaterials—a review. *J Cell Physiol* 2019;234:3321–35.
  - [14] Sendilvelan S, Bhaskar K, Nallusamy S. Experimental investigation on cerium oxide nanoparticles with alumina catalytic converter to increase emission conversion efficiency in automobiles. *Rasayan J Chem* 2017;10:460–545.
  - [15] Siddiqui SH, Higgins P, Isaac R. Alumina-based adsorbents. *Nanomaterials for environmental applications*. CRC Press; 2022. p. 161–78.
  - [16] Karamimoghdam M, Moradi M, Azami M. A comparative investigation of different overlaps of the diode laser hardening in low-carbon steel and stainless steel. *Optik* 2022;251:168093.
  - [17] Lemster K, Graule T, Kuebler J. Processing and microstructure of metal matrix composites prepared by pressureless Ti-activated infiltration using Fe-base and Ni-base alloys. *Mater Sci Eng, A* 2005;393:229–38.
  - [18] Lemster K, Graule T, Minghetti T, Schelle C, Kuebler J. Mechanical and machining properties of X38CrMoV5-1/Al<sub>2</sub>O<sub>3</sub> metal matrix composites and components. *Mater Sci Eng, A* 2006;420:296–305.
  - [19] Ning F, Hu Y, Liu Z, Wang H, Cong W, Li Y. Microstructural and mechanical performance of Al<sub>2</sub>O<sub>3</sub> nanoparticle reinforced 17-4 PH stainless steel bulk composite parts fabricated by laser engineered net shaping process. In: 2016 International solid freeform fabrication symposium; 2016.
  - [20] Koopmann J, Voigt J, Niendorf T. Additive manufacturing of a steel–ceramic multi-material by selective laser melting. *Metall Mater Trans B* 2019;50:1042–51.
  - [21] Abedi HR, Hanzaki AZ, Azami M, Kahnooji M, Rahmatabadi D. The high temperature flow behavior of additively manufactured Inconel 625 superalloy. *Mater Res Express* 2019;6:116514.
  - [22] Soleyman E, Aberoumand M, Rahmatabadi D, Soltanmohammadi K, Ghasemi I, Baniassadi M, et al. Assessment of controllable shape transformation, potential applications, and tensile shape memory properties of 3D printed PETG. *J Mater Res Technol* 2022;18:4201–15.
  - [23] Caccia M, Tabandeh-Khorshid M, Itskos G, Strayer AR, Caldwell AS, Pidaparti S, et al. Ceramic–metal composites for heat exchangers in concentrated solar power plants. *Nature* 2018;562:406–9.
  - [24] Siah Sarani A, Faraji G. Hydrostatic cyclic extrusion compression (HCEC) process; a new CEC counterpart for processing long ultrafine-grained metals. *Arch Civil Mech Eng* 2020;20:1–13.
  - [25] Shahmirzaloo A, Hosseini SM, Siah Sarani A, Rahmatabadi D, Hashemi R, Faraji G. Influences of the constrained groove pressing on microstructural, mechanical, and fracture properties of brass sheets. *Mater Res Express* 2020;7:116526.
  - [26] Alvaredo P, Escibano J, Ferrari B, Sánchez-Herencia AJ, Gordo E. Steel binder cermets processed by combination of colloidal processing and powder metallurgy. *Int J Refract Metals Hard Mater* 2018;74:1–6.
  - [27] Zhao X, Zuo D, Zhang M, Xu F, Feng S. Influence of applied pressure on the microstructure and properties of Ti (C, N)–TiB<sub>2</sub>–Co cermets prepared in situ by reactive hot-pressing. *J Ceram Soc Jpn* 2016;124:1116–22.
  - [28] Xuan W, Zhang X, Zhao Y, Li J, Wang B, Ren X, et al. Mechanism of improved intermediate temperature plasticity of nickel-base single crystal superalloy with hot isostatic pressing. *J Mater Res Technol* 2021;14:1609–17.
  - [29] Asl M, Delbari S, Azadbeh M, Namini A, Mehrabian M, Nguyen V, et al. Nanoindentational and conventional mechanical properties of spark plasma sintered Ti–Mo alloys. *J Mater Res Technol* 2020;9:10647–58.
  - [30] Koh Y, Sun J, Kim H. Freeze casting of porous Ni–YSZ cermets. *Mater Lett* 2007;61:1283–7.
  - [31] Aramian A, Razavi S, Sadeghian Z, Berto F. A review of additive manufacturing of cermets. *Addit Manuf* 2020;33:101130.
  - [32] Kazemi Z, Steeves CA. Uncertainty quantification in material properties of additively manufactured materials for application in topology optimization. *ASME Int Mech Eng Congr Expos* 2022;86656:V003T04A009.
  - [33] Arnold JM, Cramer CL, Elliott AM, Nandwana P, Babu SS. Microstructure evolution during near-net-shape fabrication of NixAl<sub>y</sub>-TiC cermets through binder jet additive manufacturing and pressureless melt infiltration. *Int J Refract Metals Hard Mater* 2019;84:104985.
  - [34] Enrique PD, Mahmoodkhani Y, Marzbanrad E, Toyserkani E, Zhou NY. In situ formation of metal matrix composites using binder jet additive manufacturing (3D printing). *Mater Lett* 2018;232:179–82.
  - [35] Rao H, Oleksak RP, Favara K, Harooni A, Dutta B, Maurice D. Behavior of yttria-stabilized zirconia (YSZ) during laser direct energy deposition of an Inconel 625-YSZ cermet. *Addit Manuf* 2020;31:100932.
  - [36] Gu D, Ma J, Chen H, Lin K, Xi L. Laser additive manufactured WC reinforced Fe-based composites with gradient reinforcement/matrix interface and enhanced performance. *Compos Struct* 2018;192:387–96.
  - [37] Sebastian R, Singh AK, Paliwal M, Gautam A. Investigation of the interface between SLM processed nickel alloy on a cast iron substrate. *Prog Addit Manuf* 2019;4:131–42.
  - [38] Carluccio D, Xu C, Venezuela J, Cao Y, Kent D, Bermingham M, et al. Additively manufactured iron-manganese for biodegradable porous load-bearing bone scaffold applications. *Acta Biomater* 2020;103:346–60.
  - [39] Wang Z, Ummethala R, Singh N, Tang S, Suryanarayana C, Eckert J, et al. Selective laser melting of aluminum and its alloys. *Materials* 2020;13:4564.
  - [40] Takata N, Liu M, Kodaira H, Suzuki A, Kobashi M. Anomalous strengthening by supersaturated solid solutions of selectively laser melted Al–Si-based alloys. *Addit Manuf* 2020;33:101152.
  - [41] Kaplanskii YY, Sentyurina ZA, Loginov PA, Levashov EA, Korotitskiy AV, Travyanov AY, et al. Microstructure and mechanical properties of the (Fe, Ni) Al-based alloy produced by SLM and HIP of spherical composite powder. *Mater Sci Eng, A* 2019;743:567–80.
  - [42] Xiang N, Xin XZ, Chen J, Wei B. Metal–ceramic bond strength of Co–Cr alloy fabricated by selective laser melting. *J Dent* 2012;40:453–7.
  - [43] Yan X, Xu YX, Wu Y, Lin H. Effects of heat treatment on metal-ceramic combination of selective-laser-melted cobalt-chromium alloy. *J Prosthet Dent* 2018;120:319:e1.
  - [44] Sing SL, Yeong WY, Wiria FE, Tay BY, Zhao Z, Zhao L, et al. Direct selective laser sintering and melting of ceramics: a review. *Rapid Prototyp J* 2017;23:611–23.
  - [45] Yu WH, Sing SL, Chua CK, Kuo CN, Tian XL. Particle-reinforced metal matrix nanocomposites fabricated by selective laser melting: a state of the art review. *Prog Mater Sci* 2019;104:330–79.
  - [46] Sercombe TB, Li X. Selective laser melting of aluminium and aluminium metal matrix composites. *Mater Technol* 2016;31:77–85.



- [47] Fang X, Yang Z, Tan S, Duan L. Feasibility study of selective laser melting for metal matrix diamond tools. *Crystals* 2020;10:596.
- [48] Singh N, Singh R, Ahuja IPS, Farina I, Fraternali F. Metal matrix composite from recycled materials by using additive manufacturing assisted investment casting. *Compos Struct* 2019;207:129–35.
- [49] Chen J, Huang M, Fang ZZ, Koopman M, Liu W, Deng X, et al. Microstructure analysis of high density WC-Co composite prepared by one step selective laser melting. *Int J Refract Met Hard Mater* 2019;84:104980.
- [50] Grigoriev S, Tarasova T, Gusarov A, Khmyrov R, Egorov S. Possibilities of manufacturing products from cermet compositions using nanoscale powders by additive manufacturing methods. *Materials* 2019;12:3425.
- [51] Campanelli SL, Contuzzi N, Posa P, Angelastro A. Printability and microstructure of selective laser melting of WC/Co/Cr powder. *Materials* 2019;12:2397.
- [52] Li Y, Bai P, Wang Y, Hu J, Guo Z. Effect of Ni contents on the microstructure and mechanical properties of TiC–Ni cermets obtained by direct laser fabrication. *Int J Refract Metals Hard Mater* 2009;27:552–5.
- [53] Enneti RK, Prough KC. Wear properties of sintered WC-12% Co processed via binder jet 3D printing (BJ3DP). *Int J Refract Metals Hard Mater* 2019;78:228–32.
- [54] Enneti RK, Prough KC. Effect of binder saturation and powder layer thickness on the green strength of the binder jet 3D printing (BJ3DP) WC-12% Co powders. *Int J Refract Metals Hard Mater* 2019;84:104991.
- [55] Xiong Y, Smugeresky JE, Schoenung JM. The influence of working distance on laser deposited WC–Co. *J Mater Process Technol* 2009;209:4935–41.
- [56] Xiong Y, Kim M, Seo O, Schoenung JM, Kang S. (Ti, W) C–Ni cermets by laser engineered net shaping. *Powder Metall* 2010;53:41–6.
- [57] Domashenkov A, Borbély A, Smurov I. Structural modifications of WC/Co nanophased and conventional powders processed by selective laser melting. *Mater Manuf Process* 2017;32:93–100.
- [58] Khmyrov RS, Shevchukov AP, Gusarov AV, Tarasova TV. Phase composition and microstructure of WC–Co alloys obtained by selective laser melting. *Mech Ind* 2017;18:714.
- [59] Han Q, Setchi R, Lacan F, Gu D, Evans SL. Selective laser melting of advanced Al–Al<sub>2</sub>O<sub>3</sub> nanocomposites: simulation, microstructure and mechanical properties. *Mater Sci Eng, A* 2017;698:162–73.
- [60] Zhang D, Cai Q, Liu J, Li R. Research on process and microstructure formation of W–Ni–Fe alloy fabricated by selective laser melting. *J Mater Eng Perform* 2011;20:1049–54.
- [61] Mercelis P, Kruth JP. Residual stresses in selective laser sintering and selective laser melting. *Rapid Prototyp J* 2006;12:254–65.
- [62] Levänen E, Mäntylä T. Effect of sintering temperature on functional properties of alumina membranes. *J Eur Ceram Soc* 2002;22:613–23.
- [63] Khmyrov RS, Safronov VA, Gusarov AV. Synthesis of nanostructured WC–Co hardmetal by selective laser melting. *Procedia IUTAM* 2017;23:114–9.
- [64] Sharan A, Cramb AW. Surface tension and wettability studies of liquid Fe–Ni–O alloys. *Metall Mater Trans B* 1997;28:465–72.
- [65] Park JS, Lee C, Park JH. Effect of complex inclusion particles on the solidification structure of Fe–Ni–Mn–Mo alloy. *Metall Mater Trans B* 2012;43:1550–64.
- [66] Chen L, Malfliet A, Zheng L, Jones PT, Blanpain B, Guo M. Densification mechanism of porous alumina plugs by molten steel with different oxygen levels. *J Eur Ceram Soc* 2018;38:2662–70.
- [67] Coble RL. Sintering alumina: effect of atmospheres. *J Am Ceram Soc* 1962;45:123–7.
- [68] Davydova A, Domashenkov A, Sova A, Movtchan I, Bertrand P, Desplanques B, et al. Selective laser melting of boron carbide particles coated by a cobalt-based metal layer. *J Mater Process Technol* 2016;229:361–6.
- [69] Ćurković L, Rede V, Grilec K, Mulabdić A. Hardness and fracture toughness of alumina ceramics. In: 12th conference on materials, processes friction and wear; 2007. p. 21–3.
- [70] Kumar S, Czekanski A. Optimization of parameters for SLS of WC–Co. *Rapid Prototyp J* 2017;23:1202–11.
- [71] Facenda JC, Borba M, Corazza PH. A literature review on the new polymer-infiltrated ceramic-network material (PICN). *J Esthetic Restor Dent* 2018;30:281–6.
- [72] Kazemi Z, Azami M. Overall mechanical properties of self-healing composites: effects of microcapsules shape, volume concentration, shell thickness, and material properties. *ASME Int Mech Eng Congr Exposit* 2022;86717:V009T12A001.